

Cluster and domain-state dynamics of ferroelectric $\text{Sr}_{1-x}\text{Ca}_x\text{TiO}_3$ ($x=0.007$)

U. Bianchi, J. Dec,* and W. Kleemann

Angewandte Physik, Gerhard-Mercator-Universität Duisburg, D-47048 Duisburg, Germany

J. G. Bednorz

IBM Forschungslaboratorium, Säumerstrasse 4, CH-8803 Rüschlikon, Switzerland

(Received 5 December 1994)

A high, rounded peak of the permittivity, $\epsilon'_{\text{max}} \approx 6 \times 10^4$, at $T \approx 18$ K evidences a percolative-type phase transition into a random-field-induced ferroelectric domain state of the doped system $\text{Sr}_{1-x}\text{Ca}_x\text{TiO}_3$ ($x=0.007$). Dispersion measurements of the permittivity reveal strong polydispersivity of the system. Deviations from Arrhenius behavior below $T=11$ K indicate the onset of dissipative quantum tunneling of the Ca^{2+} dipoles between their different off-center positions. Anomalies in both the linear and the nonlinear dielectric permittivity are explained by the presence of two different dissipative cluster contributions. They are attributed to the reorientation of Ca^{2+} -centered polar nanometer-scale regions within ferroelastic single domains of the system and to their interaction with coherent acoustic quantum fluctuations of the host lattice, respectively.

I. INTRODUCTION

Quantum paraelectrics like KTaO_3 and SrTiO_3 are well known to undergo transitions into ferroelectric low-temperature phases in the presence of small amounts of polar impurities.¹ According to measurements of the dielectric permittivity the system $\text{Sr}_{1-x}\text{Ca}_x\text{TiO}_3$ (SCT) reveals ferroelectric ordering at concentrations $x > x_{\text{cr}} = 0.0018$.² As in the cases of the related impurity systems $\text{K}_{1-x}\text{Li}_x\text{TaO}_3$ (KTL) and $\text{KTa}_{1-x}\text{Nb}_x\text{O}_3$ (KTN) off-centrality of the impurity ions is assumed. Their dipole moments polarize the host lattice, which eventually undergoes a ferroelectric instability at low enough temperatures, $T \leq T_c$.¹ In the case of SCT the spontaneous polarization lies along cubic $\langle 110 \rangle_c$ directions within the c plane of the tetragonal low- T phase. Hence, xy -type ferroelectricity with weak fourfold anisotropy is encountered.² As a result, the tetragonal D_{4h} symmetry is lowered to C_{2v} as evidenced by the splitting of the Raman active ferroelectric F_{1u} and structural E_g soft modes and by morphic birefringence.³

Rounding of the dielectric permittivity peaks, ϵ' vs T , at $x > 0.016$ (Ref. 2) and field-switchable birefringence⁴ evidence the occurrence of a random-field- (RF) induced ferroelectric domain state.⁵ It is assumed^{2,4} that the RF's are caused by randomly distributed Ca^{2+} - V_0 centers substituting Ti^{4+} - O^{2-} ion pairs. Very typically for RF pinned domain walls⁶ polydispersive extra permittivity was observed in the ferroelectric domain-state phase of SCT with $x=0.058$.⁷ Phenomenologically it was described by a Cole-Cole relaxator⁸ with a very large width of the distribution function of the relaxation times, $G(\tau)$. However, owing to an abrupt drop of the bulk permittivity at frequencies $f > 3$ kHz (presumably an artifact due to surface layers²) details of the domain-wall permittivity were obscured.

In this paper we report on novel experiments of the

complex permittivity, $\tilde{\epsilon} = \epsilon' - i\epsilon''$, of SCT with $x=0.007$ and its dependences on temperature, frequency, and applied electric fields. At $T > 20$ K the dielectric permittivity is nearly dispersionless at frequencies $10^2 < f < 3 \times 10^6$ Hz. It shows a smeared ferroelectric divergence around $T_c \approx 18$ K.³ Below T_c we observe additional polydispersive "domain-wall" permittivity, the high-frequency cutoff of which, f_0 , is related to the dynamics of the Ca^{2+} off-center dipoles. Owing to thermal activation f_0 decreases at decreasing T until crossing over into the quantum tunneling limit at $T < 11$ K.

Deeper insight into the origin of the excess permittivity is gained from the field dependence of $\tilde{\epsilon}$. In the paraelectric regime, $T > T_c$, analysis reveals two cluster contributions to $\tilde{\epsilon}$. They are due to the responses of both Ca^{2+} -centered polar clusters^{1,3} and the predicted⁹ coherent acoustic quantum fluctuations^{10,11} in addition to the permittivity of unperturbed paraelectric SrTiO_3 . The clusterlike responses persist even within the ferroelectric regime, $T < T_c$, thus corroborating on the one hand the domain-state conjecture. Nanometric 180° domains break the polar long-range order within ferroelastic 90° domains³ of micrometric size. On the other hand, the persistence of interaction with the acoustic quantum fluctuations lends support to the structural model of a percolative ferroelectric backbone embedded in an unperturbed surrounding of SrTiO_3 .

II. EXPERIMENTAL PROCEDURE

The experiments were performed on a single-crystal sample of SCT with a Ca^{2+} concentration of $x=0.007$. The value of the antiferrodistortive ($O_h \rightarrow D_{4h}$) phase-transition temperature, $T_0=125$ K, obtained from measurements of the principal ac birefringence served to determine the actual Ca^{2+} concentration of the sample. A similar value, $x=0.0053$, is obtained from the peak

temperature, $T_m = 17.6$ K, of the dielectric permittivity (see below) according to Bednorz and Müller's interpolation formula for T_m vs x .² Because of the linear dependence of T_0 on x ,³ we believe the value of x determined by birefringence to be more accurate. After x-ray orientation the sample was cut with a diamond saw and polished to optical quality with dimensions $7.5 \times 3.0 \times 0.615$ mm³ along the $[001]_c$, $[110]_c$, and $[1\bar{1}0]_c$ directions. They refer to the tetragonal (orthorhombic) c , a , and b axes below T_0 (T_c), respectively. At $T < T_c$, however, a and b are interchanging between adjacent stripe domains stacked along the c axis with average thickness $d \approx 10$ μ m.¹² For dielectric permittivity measurements it proved to be necessary to remove surface stress layers² of about 150 μ m thickness.¹³ The crystal was etched in boiling orthophosphoric acid for 3 h to yield dimensions $6.5 \times 2.6 \times 0.358$ mm³ and to form a structurally single domain sample below T_0 .¹⁴ After the etching procedure the large ac faces were covered with copper prior to vacuum deposition of gold. The complex permittivity $\bar{\epsilon} = \epsilon' - i\epsilon''$ was measured at temperatures $4.5 < T < 30$ K and frequencies $10^2 < f < 10^7$ Hz in a gas-flow cryostat along the tetragonal intraplanar easy axis b ($[1\bar{1}0]_c$) (Ref. 2) with a Hewlett-Packard 4192A impedance analyzer. Bias fields up to $E = 100$ kV/m were applied for measuring the field dependence of the permittivity, $\bar{\epsilon}$ vs E .

III. EXPERIMENTAL RESULTS AND DISCUSSION

A. Temperature dependence of the permittivity

Figure 1 shows ϵ' and ϵ'' vs T data measured within $4.5 \leq T \leq 30$ K at four frequencies, $f = 100$ Hz, 1 kHz, 10 kHz, and 100 kHz. Because of nonlinear dependences of $\bar{\epsilon}$ on increasing amplitudes E_0 of the test signal outside the Curie region at $T < 23$ K (see below) we used only $E_0 = 30$ V/m. The real part of the dielectric response ϵ' (curves 1', 2', 3', and 4'), peaks at slightly different temperatures between $T_m = 17.95$ K for low (100 Hz) and 17.55 K for high (100 kHz) frequencies. It reaches peak values $\epsilon'_{\max} \approx 60\,000$ at frequency $f = 1$ kHz of the test signal. The peaks are rounded and their half-widths increase with decreasing frequencies as a consequence of a frequency-dependent low- T shoulder. The rounding is attributed to the suppression of criticality by quenched RF's.⁵ They initiate dynamic domain freezing, which starts at about 20 K and becomes static below T_c .

As known from observations under the polarizing microscope¹² ferroelastic stripe domains with thickness 10 μ m are formed below T_c . The polarization within these stripe domains is far from being saturated. According to measurements of the linear birefringence (LB) within one single stripe domain an external electrical field of 200 kV/m is unable to saturate the polarization.⁴ The value of the LB is enhanced by a factor 3.5 at $T = 5$ K compared with zero-field measurements.¹⁵ Since the LB is sensitive to the autocorrelation function of the polarization, $\langle P^2 \rangle$, the ferroelastic stripe domains must contain a large number of polar regions that form a disordered network of ferroelectric 180° domains on a size scale well

below 1 μ m. After switching off the external field, the zero-field value of the LB is rapidly recovered due to the existence of RF's. A more detailed model of the disordered nanostructures will be discussed below in connection with nonlinear dielectric response.

Pinning of domain walls at RF's is at the origin of the low- T excess contribution to ϵ' , $\Delta\epsilon'$. The domain walls are, hence, expected⁶ to contribute polydispersively to $\bar{\epsilon}$ in particular at low temperatures. This is also reflected in the loss data, ϵ'' vs T (curves 1'', 2'', 3'', and 4''), whose peak widths at half height increase from $\Delta T = 5.3$ K at 100 kHz to $\Delta T = 9.2$ K at 100 Hz. The peak temperatures, T_p , of ϵ'' vs T shift to low T with decreasing f ($T_p = 10.2, 11.6, 13.3,$ and 15.4 K for $f = 10^2, 10^3, 10^4,$ and 10^5 Hz, respectively) with a much larger rate than T_m . Beside a "quasicritical" peak near T_m a second one, due to static domains, emerges and shifts to lower T as f decreases. A remarkable asymmetry characterizes the low- f curves. In contrast with KTN,¹⁶ the excess permittivity $\Delta\epsilon'$ has no time dependence because of the stability of the domain state in the weakly anisotropic xy system SCT.^{2,4} This contrasts with the more anisotropic Heisenberg system KTN, which relaxes towards quadrupolar long-range order at $T < T_c$.¹⁶

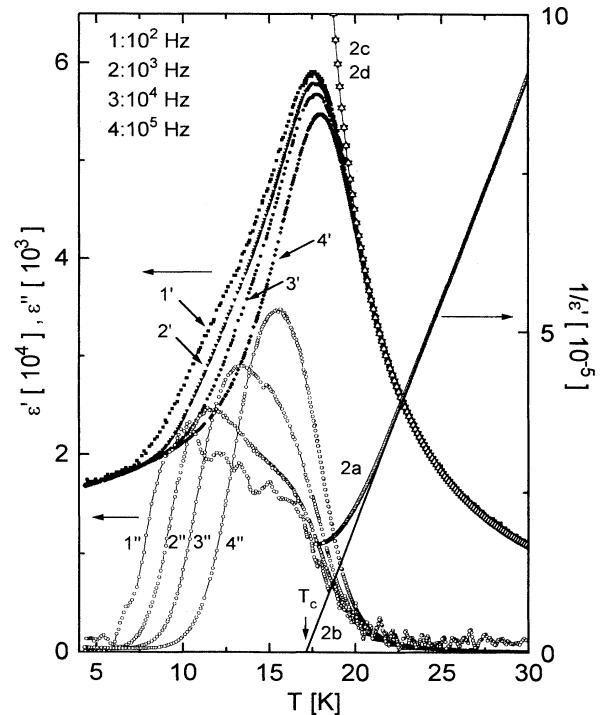


FIG. 1. ϵ' and ϵ'' of SCT ($x = 0.007$) vs temperature at various frequencies $f = 100$ Hz (1', 1''), 1 kHz (2', 2''), 10 kHz (3', 3''), and 100 kHz (4', 4''), respectively (left-hand scale). $1/\epsilon'$ for $f = 1$ kHz (2a) and best fit to Curie-Weiss law ($23 < T < 30$ K; b) with $T_c = 17.15$ K (arrow, right-hand scale). Best fits of curve 2' to power (2c) and Barrett law (2d), respectively, within $20 < T < 30$ K (see text).

In the high- T range, when fitting within $23 < T < 30$ K, ϵ' vs T shows classical Curie-Weiss-type behavior as demonstrated by the linearity of $1/\epsilon'(10^3 \text{ Hz})$ vs T in Fig. 1 (curve 2a). By extrapolation to $\epsilon'=0$ (curve 2b) it yields a Curie temperature $T_c=17.15$ K. Better fits within $20 < T < 30$ K are achieved either with a power law, $\epsilon' \propto (T-T_c)^{-\gamma}$ (Fig. 1, curve 2c with best-fit parameters $T_c=15.13$ K and $\gamma=1.26$), or with a Barrett-type¹⁷ quantum paraelectric law (Fig. 1, curve 2d),

$$\epsilon'(T) = A + B / [(T_1/2) \coth(T_1/2T) - T_0] \quad (1)$$

with best-fit parameters $A=2116$, $B=5.5 \times 10^4$ K, $T_1=75.4$ K, and $T_0=38.2$ K. Both approaches are virtually equivalent, but contrary to KTN,¹⁸ a crossover from Barrett to critical behavior cannot be observed because of the severe rounding below 20 K. Here, we only notice the similarity with the parameters found for pure SrTiO₃, $T_1=80.0$ K and $T_0=35.5$ K,¹⁹ with the subtle difference that the Ca²⁺ impurities drive T_1-2T_0 negative, a signature of ferroelectricity.

B. Dielectric dispersion

Figures 2(a) and 2(b) show the dispersion data, ϵ' and ϵ'' vs $\log_{10}f$, respectively, at $9 < T < 22$ K in a frequency range of $10^2 < f < 10^7$ Hz. Similarly as observed on SCT with $x=0.058$,⁷ the excess polydispersive permittivity, $\Delta\epsilon'$, forms very broad dispersion steps below $T \approx 22$ K. They are superimposed on the virtually constant spectrum ϵ' vs $\log_{10}f$ in the range $500 < f < 2 \times 10^6$ Hz. Upon cooling they shift towards lower f and disappear out of our present scale at $T \leq 7$ K. Their width and flat shape seems to be typical of domain-wall response under RF pinning in an external ac field.⁶ This response can be modeled by Lacroix-Béné²⁰ type distribution functions of relaxation times, $\tau=1/2\pi f$,

$$G(\ln\tau) = [\sin(\pi\beta)/\pi] [\tau_0/(\tau-\tau_0)]^\beta \quad \text{for } \tau > \tau_0 \quad (2)$$

and

$$G(\ln\tau) = 0 \quad \text{for } \tau < \tau_0.$$

τ_0 determines the fastest relaxation time (opposite to the Cole-Davidson equation²¹) and the parameter β is a measure of the polydispersity of the system. For $\beta=1$ the system behaves monodispersively. With these two parameters, τ_0 and β , the complex permittivity of polydispersive systems reads

$$\tilde{\epsilon}(\omega) = \epsilon_s - (\epsilon_s - \epsilon_\infty)(1 + 1/i\omega\tau_0)^{-\beta}, \quad (3)$$

where $\omega=2\pi f$ and ϵ_s , ϵ_∞ are the static and the very high- f limits of ϵ' , respectively. Decomposition into real and imaginary parts leads to

$$\epsilon' = \epsilon_s - (\epsilon_s - \epsilon_\infty)(\cos\lambda)^\beta \cos\lambda\beta, \quad (4a)$$

$$\epsilon'' = (\epsilon_s - \epsilon_\infty)(\cos\lambda)^\beta \sin\lambda\beta \quad (4b)$$

where $\lambda = \text{arccot}(\omega\tau_0)$.

Best fits of our data to Eqs. (4a) and (4b) are shown as solid lines in Figs. 2(a) and 2(b). The best-fit parameters are summarized in Table I. The parameters ϵ_s , β , and τ_0

are independently obtained from ϵ' and ϵ'' vs $\log_{10}f$, respectively. They agree to satisfaction at intermediate temperatures, $11 \leq T \leq 17$ K, but tend to larger deviations at $T \leq 10$ K and $T \geq 18$ K. This can be understood from

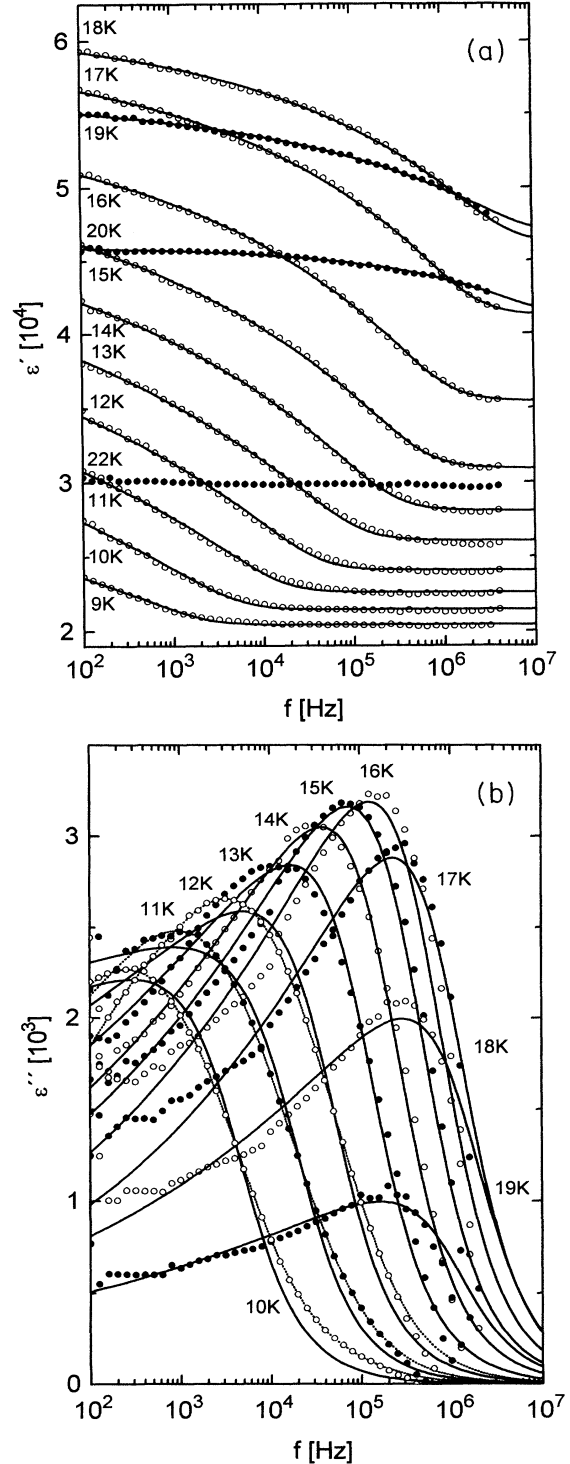


FIG. 2. ϵ' vs $\log_{10}f$ (a) and ϵ'' vs $\log_{10}f$ (b) at $9 < T < 22$ K with best fits to the Lacroix-Béné function [Eq. (4), solid lines]. Dotted lines in (b): Best fits of ϵ'' vs $\log_{10}f$ with distribution functions obtained by the histogram method (see text).

TABLE I. Best-fit parameters ϵ_S , ϵ_∞ , β , and τ_0 referring to the dispersion data ϵ' and ϵ'' (values in brackets) of Figs. 2(a) and 2(b) fitted to Eqs. (4a) and (4b), respectively.

| T (K) | ϵ_S (10^3) | ϵ_∞ (10^3) | β | τ_0 (s) |
|---------|-------------------------|------------------------------|----------------|--|
| 9 | 34.8 | 20.4 | 0.08 | 2.9×10^{-3} |
| 10 | 40.1 (58.7) | 21.5 | 0.10 (0.04) | 1.4×10^{-3} (1.5×10^{-3}) |
| 11 | 42.1 (44.4) | 22.6 | 0.11 (0.10) | 4.3×10^{-4} (3.4×10^{-4}) |
| 12 | 45.4 (45.0) | 24.1 | 0.11 (0.11) | 1.7×10^{-4} (2.5×10^{-4}) |
| 13 | 49.5 (49.6) | 26.1 | 0.10 (0.10) | 5.6×10^{-5} (5.6×10^{-5}) |
| 14 | 49.7 (49.7) | 28.1 | 0.13 (0.13) | 2.4×10^{-5} (3.0×10^{-5}) |
| 15 | 52.9 (52.3) | 30.9 | 0.13 (0.13) | 1.0×10^{-5} (1.6×10^{-5}) |
| 16 | 55.3 (55.5) | 35.4 | 0.16 (0.15) | 6.2×10^{-6} (1.0×10^{-5}) |
| 17 | 59.6 (58.5) | 41.2 | 0.18 (0.16) | 2.9×10^{-6} (6.0×10^{-6}) |
| 18 | 61.4 (60.2) | 46.2 | 0.18 (0.13) | 1.3×10^{-6} (3.9×10^{-6}) |
| 19 | 56.3 (53.5) | 46.8 | 0.17 (0.10) | 7.7×10^{-7} (5.7×10^{-6}) |
| 20 | 46.0 | 41.3 | 0.28 | 6.0×10^{-7} |

a direct inspection of the spectra displayed in Fig. 2. The loss curves in Fig. 2(b) are clearly truncated in the low- and high- f regions for $T \leq 10$ K and $T \geq 18$ K, respectively. Hence, poor reliability of their fitting parameters may be anticipated. On the other hand, the relatively low noise found in the ϵ' vs $\log_{10}f$ curves in Fig. 2(a) makes

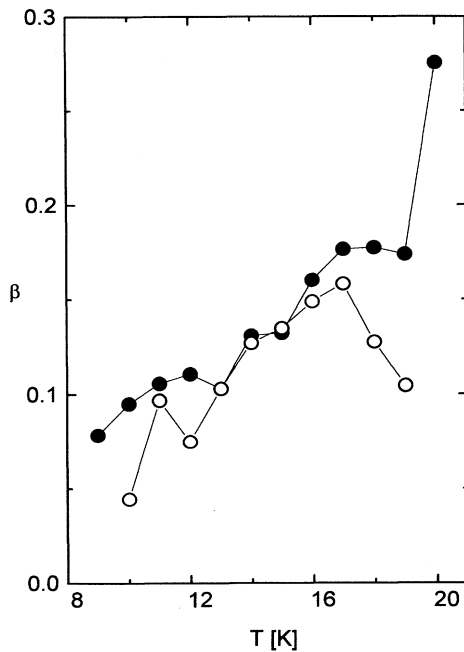


FIG. 3. Parameter β vs T obtained from best fits in Fig. 2 of ϵ' (solid circles) and ϵ'' (open circles) to Lacroix-Béné-type functions [Eq. (4)] interpolated by straight lines.

their fits more reliable even for the marginal temperatures quoted above. Thus we are inclined to prefer the parameters obtained from Fig. 2(a). This is, e.g., corroborated by the reasonable monotonic behavior of β vs T as shown in Fig. 3 (solid circles), whereas the nonmonotonic decrease of β vs T as obtained from ϵ'' vs $\log_{10}f$ at $T > 17$ K (open circles) should be cast in doubt. Similarly, Arrhenius plots of $\ln(f_0/\text{Hz})$ vs $1/T$, where $f_0 = 1/2\pi\tau_0$, in Fig. 4 reveal much lower scatter for the data originating from ϵ' (solid circles) compared with those from ϵ'' (open circles). Hence, our analysis focuses on the evaluation of ϵ' vs $\log_{10}f$. The corresponding distribution functions, Eq. (2), are shown in Fig. 5. They clearly reveal the strongly T -dependent high- f cutoff and the increasing importance of the low- f tail as T decreases.

Figure 6 shows Cole-Cole plots of the dispersion data, ϵ'' vs ϵ' , referring to Figs. 2(a) and 2(b). Their high-frequency cutoff values, ϵ_∞ , clearly mark the ferroelectric peak at $T \sim 18$ K and its subsequent decrease as T decreases (Fig. 1). The polydispersity of the system under investigation is, again, obvious from the considerable flattening of the semicircles. Similarly, as observed on KTL,^{22,23} virtually infinite slopes are observed at high frequencies, whereas finite slopes determine the low-frequency branches. In accordance with the tremendous decrease of the exponent β (Fig. 3) the extrapolated semicircles become extremely flat at low T . Unfortunately large parts of them are lacking experimental confirmation owing to the extreme slowing down of the dielectric response. Closer inspection shows that a second flattened

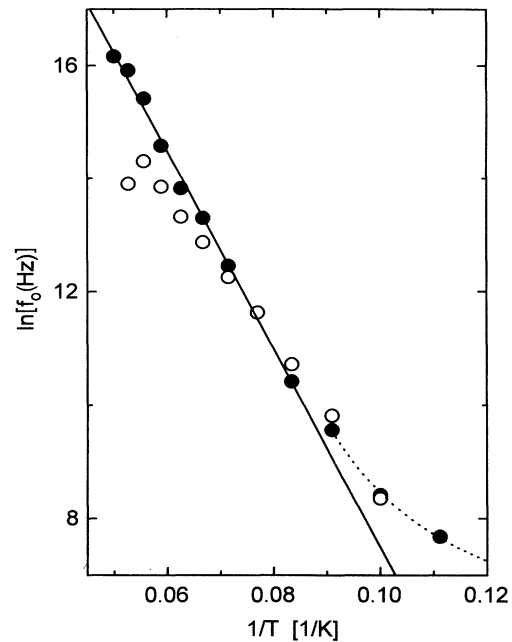


FIG. 4. Arrhenius plot of cutoff frequencies f_0 of Lacroix-Béné distributions (Fig. 5, solid lines) fitted to ϵ' (solid circles) and to ϵ'' (open circles) vs $\log_{10}f$, respectively. Solid line: best fit of $\ln f_0(\epsilon')$ vs $1/T$ to Arrhenius law. Dashed line: best fit to quartic quantum tunneling parabola (see text).

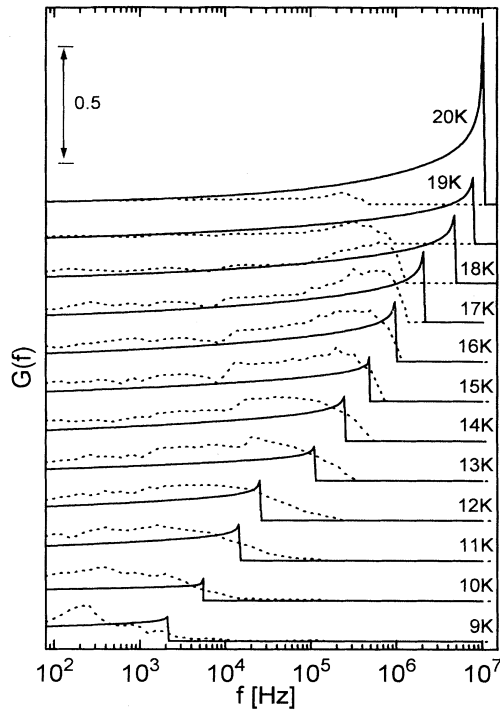


FIG. 5. Distribution functions $G(f)$ of relaxation times of SCT ($x = 0.007$) according to best fits of Eq. (4a) (solid lines) to ϵ'' vs $\log_{10}f$ [Fig. 2(a)] and according to the histogram method (dashed lines) applied to ϵ'' vs $\log_{10}f$ [Fig. 2(b)]. The scale refers to the solid lines.

Cole-Cole semicircle probably appears in the high- ϵ' , low- f region as T approaches $T_c \approx 18$ K (arrows in Fig. 6). It seems to correspond to the “quasicritical” peak observed in ϵ'' vs T (Fig. 1) and is connected (see below) with the “soft cluster” response due to coherent acoustic quantum fluctuations.^{9,11}

The complex structure of the ϵ'' vs ϵ' plots (Fig. 6) and the non-negligible deviations of the experimental data from the crude distribution function, Eq. (2) (Figs. 2 and 6), clearly demand for a more sophisticated analysis. As a first step it is customary to parametrize the dielectric data in terms of a distribution of relaxation times, $G(\ln\tau)$. This approach assumes the system consists of noninteracting Debye-type relaxators. It is, hence, of limited value in strongly interacting cluster systems like ferroelectric SCT. A model theory based on Glauber dynamics of randomly interacting pseudospins has recently²³ been applied to the relaxing KTL system. The strophoidal shape of the Cole-Cole diagrams was successfully reproduced. The Lacroix-Béné-type distribution function turns out to be a simplified special case. However, since important qualitative features have not yet fully been understood, we shall not use this formalism, but rather restrict ourselves to the formal deduction of $G(\ln\tau)$.

By use of the histogram method of Imanishi *et al.*²⁴ we have calculated $G(\ln f)$ from our data ϵ'' vs $\log_{10}f$ [Fig. 2(b)]. They are plotted in comparison with the Lacroix-Béné-type functions, Eq. (2), in Fig. 5. Some common features, but also differences, are obvious. Both types of

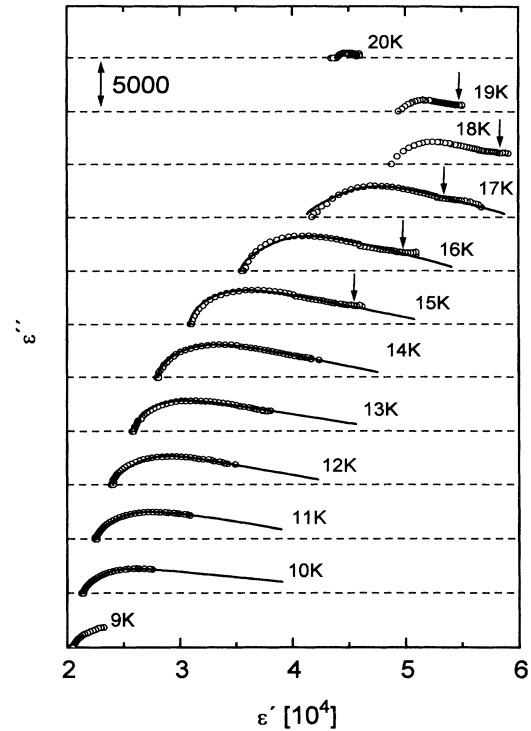


FIG. 6. Cole-Cole plots ϵ'' vs ϵ' of experimental data (open circles, see Fig. 2) and their best fits to the Lacroix-Béné function (solid lines) for $9 < T < 20$ K with dashed horizontal lines referring to $\epsilon'' = 0$. Arrows indicate additional Cole-Cole semicircles at $T \approx T_c$.

distribution functions show low- f tails, which seem to extend to $f = 0$ for low T . This qualifies the response to be quasi-glass-like.²² The cutoff frequency shifts to higher values with increasing T and follows an Arrhenius law (see below) at $T > 11$ K. In contrast with the analytical Lacroix-Béné distributions the “real” distributions do not show abrupt cutoffs. They are smeared out to high frequencies, thus improving the fits to ϵ'' vs $\log_{10}f$ in the high- f limit [Fig. 2(b), dashed lines]. However, for $T > 16$ K sharp cutoffs are also found in the “real” distribution functions. This is probably an artifact due to poor data quality at $f > 10^6$ Hz, which also gives rise to erroneous β parameters (Fig. 3) and $\ln f_0$ values (Fig. 4).

Linear regression of the $\ln f_0$ data obtained from ϵ'' vs $\log_{10}f$ in the range $12 \leq T \leq 20$ K (Fig. 4, solid line) yields an Arrhenius function $\ln(f_0/\text{Hz}) = \ln(f_\infty/\text{Hz}) - \Delta E/k_B T$ with an activation energy $\Delta E/k_B = (175 \pm 4)$ K and a hopping frequency limit of $f_\infty = (7 \pm 1) \times 10^{10}$ Hz. These values compare well with those reported for SCT with $x = 0.002$.¹¹ As discussed there, the quantities ΔE and f_∞ are considered as thermodynamical properties of the whole ensemble of interacting Ca^{2+} dipoles thus averaging out local properties like individual barrier heights and local phonon frequencies. At $T < 11$ K deviations from the Arrhenius behavior are observed. The $\ln f_0$ values lie above the Arrhenius line and seem to saturate in the $T \rightarrow 0$ limit. This behavior hints at the onset of dissipative quantum tunneling of the Ca^{2+} dipoles be-

tween the potential minima in the four-well potential. Similar behavior was observed in the related system KTL ($x_{Li}=0.011$) at $T < 20$ K.²⁵ Owing to the strong interaction of the reorienting impurity dipoles with acoustic phonons the well-known T^4 law²⁶ of the relaxation time in the phonon-assisted dissipative quantum tunneling regime is expected to hold. The data are, indeed, quite satisfactorily fitted by the parabola $\ln(f_0/\text{Hz})=6.1+2.3 \times 10^{-4} (\text{T/K})^4$ (Fig. 4, dashed line), hence, $f_0(T=0)=445$ Hz. It will be interesting to confirm experimentally the saturation of $f_0(T)$ at very low temperatures and to compare $f_0(0)$ with theoretical predictions relying on the concept of dissipative quantum tunneling.²⁷

C. Electric-field dependence of the permittivity

As indicated by the complex structure of the Cole-Cole diagrams (Fig. 6) and of the realistic distribution function $G(\ln\tau)$ (Fig. 5) there are at least two different contributions to the polydispersive excess permittivity, $\Delta\epsilon'$. This is corroborated in a much clearer way by a novel analysis of the nonlinear behavior of ϵ' as obtained from its field dependence, ϵ' vs E , at fixed temperature, T , and frequency, $f=10$ kHz. As shown in Fig. 7, these functions reveal monotonic curvature at high temperatures, $T \geq 30$ K, whereas inflexion points appear on cooling to below 25 K. They separate a steep initial decrease from weak monotonic high-field decrease at fairly low fields, $E \approx 30$ kV/m.

Owing to hysteresis the ϵ' vs E [Fig. 7(c) inset] or $P(E)=\epsilon_0 \int_0^E \epsilon'(E')dE'$ vs E loops (Fig. 8) are slightly nonergodic at $T \leq 20$ K. Slim S-shaped hysteresis loops are observed throughout the ferroelectric regime, $T \leq 18$ K (Fig. 8). Both the remanences, $P(E=0)$, and the coercive fields, $E(P=0)$, are extraordinarily small when compared with conventional ferroelectrics like BaTiO₃ or TGS.²⁸ At first glance this might be traced back to the rare fact of nearly vanishing quartic anisotropy of the easy-plane xy -type ferroelectric SCT.² Coercivity as probed by 180° domain switching in an external ac field is merely due to RF pinning as will be discussed in more detail in Sec. III D. At closer look, however, the lack of saturation and rectangularity of the P vs E curves even at $T < 10$ K (Fig. 8) is highly surprising. Their rounded shape even at $T=4.5$ K seems to evidence superparaelectric rather than ferroelectric behavior. In fact, this idea will be at the heart of the forthcoming discussion, which concentrates, however, on the original ϵ' vs E curves (Fig. 7).

Disregarding the above-mentioned nonergodicity we inspect ϵ' vs E as recorded at decreasing E after first sweeping up to $E=100$ kV/m. Obviously, conventional analysis of ϵ' vs E involving merely even powers of E as recently applied to SCT with $x=0.003$ and 0.004 (Ref. 29) fails to explain this behavior. Only conventional nonlinear (nl) response can be described by such a power series. In order to explain the semi-bell-shaped curves in Fig. 7 we propose¹¹ that important contributions due to the reorientation of the off-center Ca²⁺ dipoles have to be

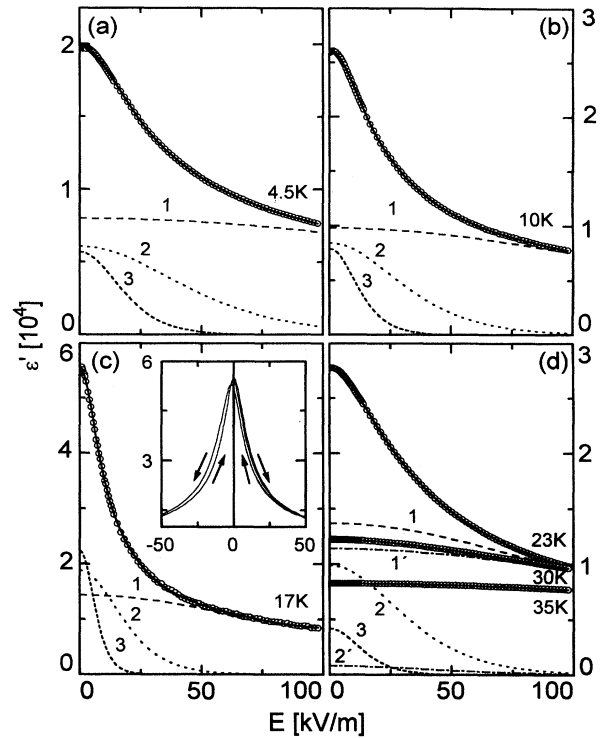


FIG. 7. ϵ' vs bias field E (open circles) at $f=10$ kHz and temperatures $T=4.5$ (a); 10 (b); 17 (c); and 23, 30, and 35 K (d) and best fits (solid lines) to Eq. (6) decomposed into lattice (curves 1 and 1') and cluster contributions (curves 2, 2' and 3, 3', respectively). In (d), curves 1–3 and 1'–2' refer to $T=23$ and 30 K, respectively. The inset of (c) shows a virgin curve and a subsequent complete cycle of ϵ' vs E indicated by arrows.

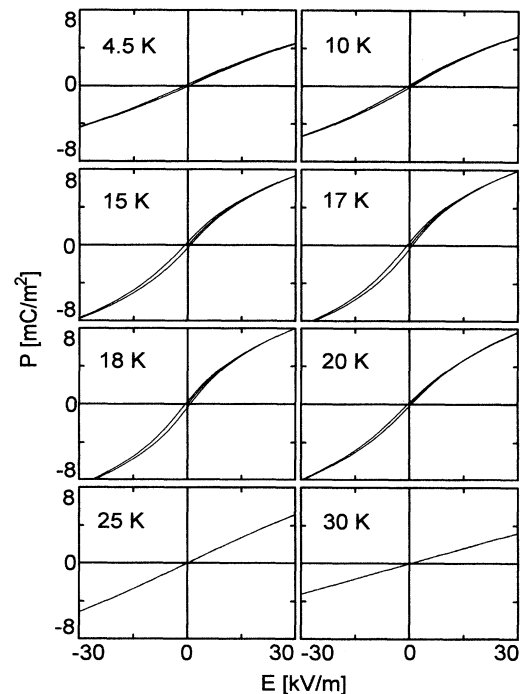


FIG. 8. P vs E hysteresis cycles as calculated from ϵ' vs E cycles [cf. Fig. 7(c) inset] at various temperatures, $4.5 \leq T \leq 30$ K.

taken into account. By use of a Langevin-type approach³⁰ the total polarization of a cluster system with four different possible orientations of the Ca^{2+} dipoles within the (001) plane is calculated to be

$$P_c = P_r \tanh(P_r L^3 E / 2k_B T) \quad (5)$$

with the effective polarization of one cluster P_r , cluster size L , electric field E , and Boltzmann's constant k_B . Inspection shows that two clusters with different reorientation contributions, $(1/\epsilon_0)(\partial P_c / \partial E)$, are needed to describe the field dependence of the permittivity in addition to conventional nl contributions:

$$\begin{aligned} \epsilon'(E) = & \epsilon'_1 - \epsilon'_2 E^2 + \epsilon'_3 E^4 \\ & + \sum_{j=1}^2 (P_j x_j / \epsilon_0) [\cosh(Ex_j)]^{-2}, \end{aligned} \quad (6)$$

where $x_j = P_j L_j^3 / (2k_B T)$ with the cluster polarizations P_j and diameters L_j . $\epsilon'_{1,2,3}$ and ϵ_0 designate the linear, nl, and higher-order permittivities and that of the vacuum, respectively. It should be noticed that, similar to the case of SCT $x = 0.002$,¹¹ a significantly worse fit emerges assuming only one cluster contribution in addition to the bulk response. The contributions to ϵ' are interpreted as follows.

The three leading terms in Eq. (6) describe the conventional linear and nl response up to order E^4 [Figs. 7(a)–7(d), curves labeled as 1, and as 1' and 35 K in Fig. 7(d)]. They correspond to the conventional field dependence of ϵ' of displacive-type polar systems in the paraelectric regime. It turns out that this description also remains valid below T_c in our system. This hints at a paraelectric background persisting at all temperatures as observed, e.g., for pure SrTiO_3 . This interpretation will be reinforced below.

The sum in Eq. (6) describes two contributions due to the reorientation of Ca^{2+} centered clusters. “Hard” clusters give contributions to ϵ' up to fields $E = 100$ kV/m [Figs. 7(a)–7(d), labeled as 2]. They are tentatively attributed to the polar nanometer-scale regions. Their contribution to the permittivity at $E = 0$ is about 30% for temperatures below 25 K. At $T > 25$ K this response decays rapidly (see also Fig. 9, curve denoted as P_1) with increasing temperatures and is absent at $T \geq 35$ K. The polar nanometer-scale regions carry constant polarization, $P_1 \approx 3.3$ mC/m² below $T \approx 25$ K (Fig. 9). The mesoscopic cluster size, $L_1 \approx 10$ –20 nm (Fig. 9, curve denoted as L_1), compares favorably with general expectations of RF controlled nanometer-scale domains.⁵ In our case at a Ca^{2+} concentration $x = 0.007$ they contain some 30–300 individual Ca^{2+} dipoles together with their polarization clouds. Hence, it is very likely that different cluster (=nanometer-scale domain) orientations result from the subtle balance between dipolar energy gain due to spatial fluctuations of the RF's and domain-wall energy loss including elastic contributions. In accordance with the theory of RF controlled domains in systems with narrow domain walls^{31,32} we find approximate linearity, $L_1 \propto T$, of the cluster size with temperature at $T \leq T_c \approx 18$ K.

The “soft” cluster contribution to the permittivity ap-

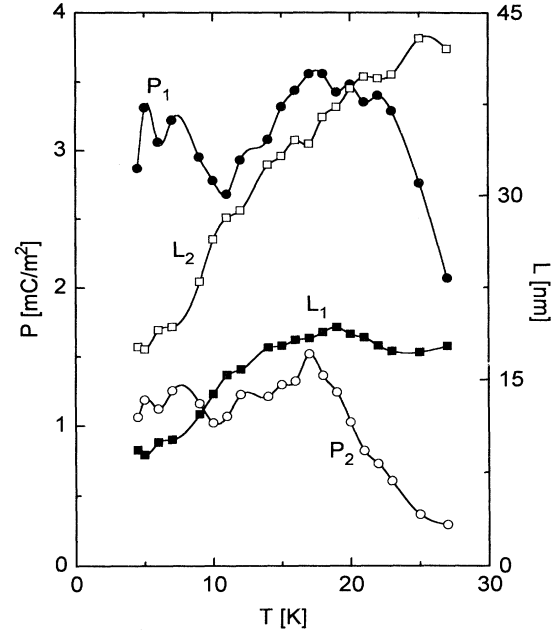


FIG. 9. Temperature dependences of cluster polarizations (P_i , left-hand scale) and correlation lengths (L_i , right-hand scale) obtained by best fits of ϵ' vs E (Fig. 7) to Eq. (6) and connected by eye-guiding solid lines. The indices refer to “hard” (1) and “soft” clusters (2) (see text).

pears at $T < 25$ K and reaches about 30% at $E = 0$ and low T [Figs. 7(a)–7(d), curves labeled as 3]. At low fields it is as important as that of the “hard” clusters, but rapidly decreases with increasing bias fields. For $E > 50$ kV/m the “soft” cluster response disappears. In the vicinity of T_c [Fig. 7(c)] and at small fields ($E < 10$ kV/m) reorientation contributions of both kinds of clusters are more important than the conventional dielectric permittivity due to displacements. The response of the “soft” clusters is very probably due to coherent acoustic quantum fluctuations,⁹ which interact electrostrictively with the polar nanoregions.¹¹ Its high sensitivity to electrical fields seems to corroborate a prediction of Vikhniin,³³ who conjectures coherent acoustic quantum fluctuations to originate from tunnel excitations of the multipotential well system of the host lattice. These fluctuations may be represented by wave packets traveling through the sample with σ_{xy} stress components, which excite P_x components via the piezoelectric modulus $d_{15} \neq 0$ in polar regions with $mm2$ symmetry ($x \parallel [110]_c$, $z \parallel [001]_c$).

The “soft” clusters carry constant polarization $P_2 \approx 1.2$ mC/m² below T_c (Fig. 9). Above T_c the polarization decays nearly linearly with increasing temperatures and vanishes at $T \approx 30$ K (Fig. 9), hence, close to the “transition temperature,” $T_q \approx 37$ K, into the predicted “coherent quantum state.”⁹ The correlation length L_2 of the “soft” clusters decreases with decreasing T from 45 nm at 30 K to 15 nm at 5 K. This can be understood by considering that the acoustic shear waves exclusively originate from undistorted regions of “pure” SrTiO_3 . These become progressively smaller as the ferroelectric

percolating network increases its compactness upon saturating at low temperatures. Hence, L_2 is a measure of the “free volume” between the polar nanoregions.

Figure 10 shows the T dependences for ϵ'_1 , ϵ'_2 , and ϵ'_3 obtained from the best-fit procedures of our ϵ' vs E data (Fig. 7) to Eq. (6). They are described by Curie-Weiss laws, $\epsilon'_i = C_i / (T - T_{c,i})^{\gamma_i}$, with individual Curie temperatures $T_{c,i}$, constants C_i , and critical exponents γ_i . According to the classical theory one expects $\gamma_1=1$, $\gamma_2=4$, and $\gamma_3=7$.³⁴ Corresponding best fits (solid lines in Fig. 10) are quite satisfactory at $T > 20$ K albeit yielding unexpectedly low Curie temperatures $T_c = 4.2$, 1.9, and -0.8 K referring to ϵ'_1 , ϵ'_2 , and ϵ'_3 vs T , respectively. Obviously, quasiparaelectric behavior with $T_c \approx 0$ is observed for all of the “bulk” susceptibilities, ϵ'_1 , ϵ'_2 , and ϵ'_3 . This is at variance with the Curie-Weiss ($T_c \approx 15$ K, $\gamma_1 \approx 1.3$) or Barrett-type behavior ($T_1/2T_0 = 0.98$) of the total permittivity, ϵ' vs T , as discussed in Sec. III A (Fig. 1, curves 2c and d). In fact, the decomposition of ϵ' vs T into conventional (“bulk”) and additional cluster contributions suggested by Eq. (6) obviously discerns between a paraelectric background response and that of the polar nanoregions. The conventional contributions should, hence, behave similarly as pure SrTiO₃. Clearly, this holds for $T > T_c$ only. Below the phase-transition temperature all of the SrTiO₃-like contributions, ϵ'_1 , ϵ'_2 , and ϵ'_3 , decrease approximately linearly with T (Fig. 10, dashed lines) thus reacting to the increasing compactness of the ferroelectric cluster network. It should be noticed that a Barrett-type description instead of the Curie-Weiss law can be chosen for the T dependence of ϵ'_1 . We find

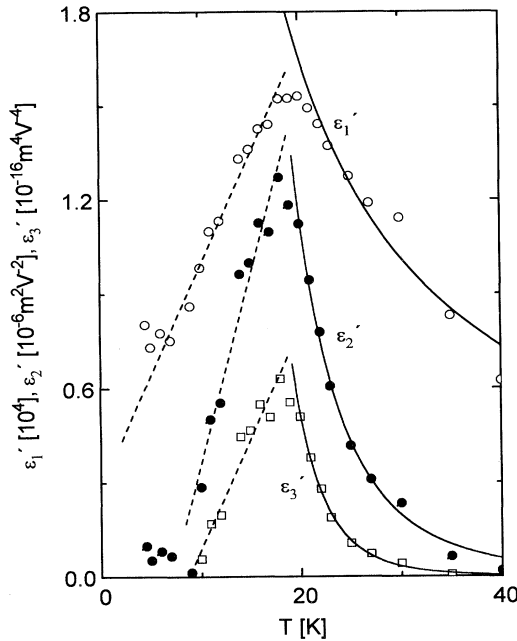


FIG. 10. Linear (ϵ'_1), nonlinear (ϵ'_2), and higher-order (ϵ'_3) permittivities vs T obtained from the analysis of ϵ' vs E (Fig. 7) best-fitted to Curie-Weiss laws at $T > 20$ K (solid lines, see text) and to linear functions at $T < 18$ K (dashed lines).

$T_1 = 79$ K and $T_0 = 36$ K, both of which are close to the values observed for pure SrTiO₃.¹⁹

The peak of ϵ' vs T (Fig. 1) is due to the ferroelectric instability and primarily reflects the static polar distortion of the Ca²⁺ centered nanoregions. On applying external electrical fields the local potential wells of the off-center Ca²⁺ dipoles are stabilized. This causes the ϵ' peak to shift to higher T as E increases as shown in Fig. 11. The ϵ' vs T curves labeled as 1a, 2, 3, 4, 5, 6, and 7 are recorded at $f = 1$ kHz with bias fields $E = 0, 2.5, 5, 10, 20, 40,$ and 80 kV/m, respectively. From an analysis of the Landau-Devonshire free-energy expansion including the lowest-order nonlinear dielectric term one expects the shift of the peak temperature, $\Delta T_m = T_m(E) - T_m(0)$, of ϵ' on E is dominant, ΔT_m should vary with E^2 above T_c .²⁸ This agrees with our experimental results for $E < 5$ kV/m, whereas $E^{2/3}$ behavior prevails at $E > 5$ kV/m as shown in the inset of Fig. 11. In parallel to the shift of T_m with increasing E the peak values of ϵ' gradually decrease from 66 000 for $E = 0$ (Fig. 11, curve 1a) to 11 000 for $E = 80$ kV/m (curve 7). Similar behavior was observed for pure SrTiO₃ (Ref. 35) and is generally predicted for ferroelectrics.³⁶

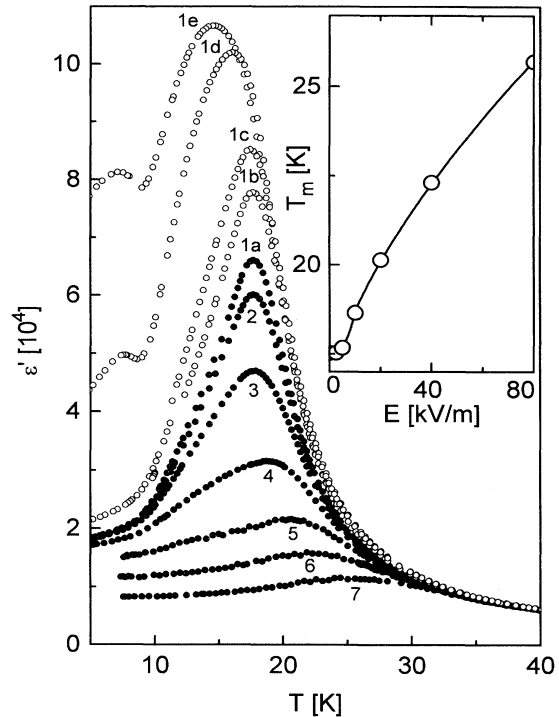


FIG. 11. ϵ' vs T measured at $f = 1$ kHz with constant bias fields $E = 0$ (1a–e), 2.5 (2), 5 (3), 10 (4), 20 (5), 40 (6), and 80 kV/m (7) and with different amplitudes of the test signal $E_0 = 30$ V/m (1a–b, 2–7), 300 V/m (1c), 1.5 kV/m (1d), and 3 kV/m (1e). Inset: Peak temperatures T_m vs E (open circles) together with fits (solid line) $T_m \propto E^2$ for $E < 5$ kV/m and $T_m \propto E^{2/3}$ for $E > 5$ kV/m.

D. Amplitude dependence of the permittivity

It is interesting to notice that the permittivity does not only depend on the value of an applied bias field E , but also on the amplitude E_0 of the ac test signal. This is demonstrated for $E=0$ in Fig. 11, which shows ϵ' vs T for various amplitudes, $0.03 \leq E_0 \leq 3$ kV/m (curves 1a–1e) and in Fig. 12, which shows ϵ' and ϵ'' vs E_0 at various temperatures, $5 \leq T \leq 25$ K. Whereas virtually no dependence on E_0 is observed in the paraelectric Curie region, $T \geq 22$ K, we find significant enhancements of both ϵ' and ϵ'' after passing the phase transition, $T \leq 19$ K. Record values as large as $\epsilon' = 1.1 \times 10^5$ occur at $T = 16$ K with $E_0 > 1.5$ kV/m. Similar values seem achievable at lower temperatures, $T = 12$ K, where our maximum amplitude $E_0^{\max} = 2.8$ kV/m, reveals an unsaturated value $\epsilon' = 1.0 \times 10^5$. Simultaneously, the relative change with E_0 of the dielectric loss, $N = \epsilon''(E_0^{\max})/\epsilon''(E_0 \approx 0)$, increases considerably as T is lowered. Whereas $N \approx 2$ for $T = 19$ K $\approx T_c$, we find $N \approx 30$ for $T = 5$ K. It should be noticed that all of these data are slightly history dependent. This is clearly suggested by the hysteretic effects shown in Fig. 12. Aging is evident from curves 1a and b in Fig. 11, which were measured with identical field parameters ($E=0$ and $E_0=30$ V/m) on the freshly prepared virgin sample (curve 1b) and after

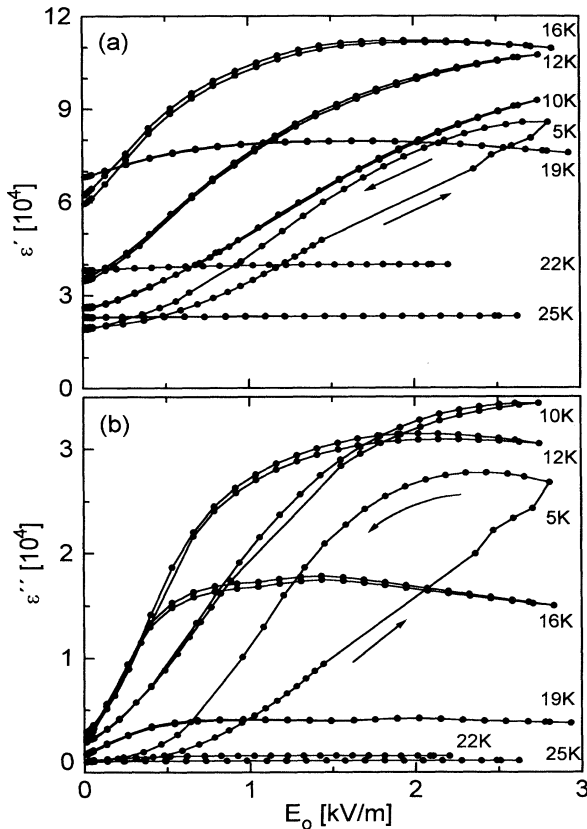


FIG. 12. (a) ϵ' and (b) ϵ'' vs test signal amplitude E_0 at $f = 1$ kHz and various temperatures $T \leq T \leq 25$ K connected by eye-guiding lines. Hysteretic cycles are indicated by arrows.

3 months time and numerous temperature and field cycles (curve 1a), respectively. Nonsaturation of both ϵ' and ϵ'' for fields $E_0 \leq E_0^{\max}$ is typical of the low- T regime, $T \leq 12$ K, whereas saturation is achieved at intermediate values, $E_0 < E_0^{\max}$, for the higher- T range.

The dependence on E_0 of $\bar{\epsilon}$ is clearly a domain state feature. Domain-wall pinning at spatial fluctuations of the RF's suppresses the critical divergence of ϵ' at T_c and, simultaneously, gives rise to a small, but finite hysteresis of the polarization, P vs E (Fig. 8). A similar hysteresis loop is probed by the low ac field within $-E_0 \leq E \leq E_0$ when measuring $\bar{\epsilon}$. Its average slope, dP/dE , is a measure of ϵ' , whereas its area, $\oint P dE$, determines the dielectric loss, ϵ'' . Quite generally the average slope is fairly small when probing a virgin domain state with an amplitude below the wall depinning threshold. It increases above this threshold, but decreases again when approaching saturation via nonlinearity [cf. second term in Eq. (6)]. These features qualitatively apply to our observations in the vicinity of T_c (Fig. 12, $T = 16$ and 19 K). At lower T the depinning fields increase beyond our present limit of E_0 . Hence, saturation is not available. In addition, the curves ϵ' and ϵ'' vs E become hysteretic. This is most drastically realized at $T = 5$ K (Fig. 12). The domain walls, depinned by increasing amplitudes remain mobile at subsequent decrease of E_0 . Probably this is a consequence of field-induced domain-wall smoothing, which gives rise to less "friction" due to pinning. Thus the values of the susceptibility measured at decreasing amplitudes are enhanced compared with the initial ones recorded at increasing amplitudes (Fig. 12).

IV. SUMMARY

Measurements of the temperature dependence of the permittivity show a smeared ferroelectric divergence at $T_c \approx 18$ K. It evidences a percolative-type phase transition into a RF-induced ferroelectric domain state. Low- T excess contributions to both the real and the imaginary parts of the permittivity are attributed to pinning of domain walls at RF's. The validity of both a classical Curie-Weiss law and a Barrett-type description fails below $T \approx 23$ K, about 5 K above the phase transition. This reflects the presence of ferroelectric nanoregions above T_c , as evidenced previously by Raman spectroscopy.³

The dispersion data of the permittivity reveal strong polydispersivity of SCT and give additional support to the model of domain wall pinning at RF's. The temperature dependence of the high-frequency cutoffs of the relaxation frequency distribution functions follows an Arrhenius law for $T > 11$ K and yields an activation energy of $\Delta E/k_B = 175$ K. Below $T = 11$ K significant deviations from the Arrhenius line hint at crossover into the dissipative quantum tunneling regime.

Analysis of the permittivity data as a function of an electric bias field reveal additional contributions due to reorienting polarization of two types of different clusters in addition to the conventional response of the polarization. One of

these clusters corresponds to the ferroelectric nanometer-scale domains, whereas the second cluster contribution represents a novel energy dissipative process. It is proposed to be due to the presence of coherent acoustic quantum fluctuations interacting with the nano-domain system. Within the framework of our model the conventional response of the permittivity seems to be due to the unperturbed host lattice of SrTiO₃.

The dependences on both the bias field E and the ac test amplitude E_0 evidence strong nonlinear response of the polarization on applied electrical fields below T_c . They lend further support to our model of ferroelectric SCT. The inherent disorder of the percolating network of polar nanodomains (180° domains) is due to RF pin-

ning forces, which give rise to extremely narrow hysteresis loops and dissipation.

ACKNOWLEDGMENTS

This work was supported by research grants of the DAAD and the Polish Committee for Scientific Research to one of us (J.D.) and by the Deutsche Forschungsgemeinschaft via Forschungsschwerpunkt "Pseudosymmetrische Kristalle." J.D. thanks for the hospitality during his stay at the Laboratory of Applied Physics, University of Duisburg. Discussions with V. S. Vikhnin are gratefully acknowledged.

*Permanent address: Institute of Physics, University of Silesia, Katowice, Poland.

- ¹B. E. Vugmeister and M. D. Glinchuk, *Rev. Mod. Phys.* **62**, 993 (1990).
- ²J. G. Bednorz and K. A. Müller, *Phys. Rev. Lett.* **52**, 2289 (1984).
- ³U. Bianchi, W. Kleemann, and J. G. Bednorz, *J. Phys. Condens. Matter* **6**, 1229 (1994).
- ⁴W. Kleemann, F. J. Schäfer, K. A. Müller, and J. G. Bednorz, *Ferroelectrics* **80**, 297 (1988).
- ⁵For a review see W. Kleemann, *Int. J. Mod. Phys. B* **7**, 2469 (1993).
- ⁶T. Nattermann, Y. Shapir, and I. Vilfan, *Phys. Rev. B* **42**, 8577 (1990).
- ⁷W. Kleemann and H. Schremmer, *Phys. Rev. B* **40**, 7428 (1989).
- ⁸K. S. Cole and R. H. Cole, *J. Chem. Phys.* **9**, 341 (1941).
- ⁹K. A. Müller, W. Berlinger, and E. Tosatti, *Z. Phys. B* **84**, 277 (1991).
- ¹⁰E. Courtens, G. Coddens, B. Hennion, B. Hehlen, J. Pelous, and R. Vacher, *Phys. Scr. T* **49**, 430 (1993).
- ¹¹J. Dec, W. Kleemann, U. Bianchi, and J. G. Bednorz, *Europhys. Lett.* **29**, 31 (1995).
- ¹²U. Bianchi, W. Kleemann, and J. G. Bednorz, *Ferroelectrics* **157**, 165 (1994).
- ¹³K. Aso, *Jpn. J. Appl. Phys.* **15**, 1243 (1976).
- ¹⁴K. A. Müller, W. Berlinger, M. Capizzi, and H. Gränicher, *Solid State Commun.* **8**, 549 (1970).
- ¹⁵M. Prasse, Diploma thesis, Universität Duisburg, 1993.
- ¹⁶A. Klössner, U. A. Leitão, W. Kleemann, and D. Rytz, *Ferroelectrics* **157**, 245 (1994).
- ¹⁷H. Barrett, *Phys. Rev.* **86**, 118 (1952).
- ¹⁸R. Kind and K. A. Müller, *Commun. Phys.* **1**, 223 (1976).
- ¹⁹K. A. Müller and H. Burkard, *Phys. Rev. B* **19**, 3593 (1979).
- ²⁰R. P. Lacroix and G. J. Béné, *Arch. Sci.* **4**, 430 (1951).
- ²¹D. W. Davidson and R. H. Cole, *J. Chem. Phys.* **18**, 1417 (1950).
- ²²F. Wickenhöfer, W. Kleemann, and D. Rytz, *Ferroelectrics* **124**, 327 (1991); **135**, 333 (1992).
- ²³P. Doussineau, Y. Farssi, C. Frénois, A. Levelut, K. MacEnaney, J. Toulouse, and S. Ziolkiewicz, *Phys. Rev. Lett.* **70**, 96 (1993); P. Doussineau, Y. Farssi, C. Frénois, A. Levelut, J. Toulouse, and S. Ziolkiewicz, *J. Phys. I (France)* **4**, 1217 (1994).
- ²⁴Y. Imanishi, K. Adachi, and T. Kotaka, *J. Chem. Phys.* **89**, 7593 (1988).
- ²⁵W. Kleemann, V. Schönknecht, and D. Rytz, *Phys. Rev. Lett.* **66**, 762 (1991).
- ²⁶H. Grabert and U. Weiss, *Phys. Rev. Lett.* **53**, 1787 (1984).
- ²⁷A. O. Caldeira and A. J. Leggett, *Phys. Rev. Lett.* **46**, 211 (1981); H. Grabert, U. Weiss, and P. Hänggi, *Phys. Rev. Lett.* **52**, 2193 (1984).
- ²⁸M. E. Lines and A. M. Glass, *Principles and Applications of Ferroelectric and Related Materials* (Clarendon, Oxford, 1979), p. 169.
- ²⁹M. Maglione, M. Lopes dos Santos, M. R. Chaves, and A. Almeida, *Phys. Status Solidi B* **181**, 73 (1994).
- ³⁰A. J. Bell, *J. Phys. Condens. Matter* **5**, 8773 (1993).
- ³¹J. Villain, *Phys. Rev. Lett.* **52**, 1543 (1984).
- ³²T. Nattermann, *Ferroelectrics* **104**, 171 (1990).
- ³³V. S. Vikhnin, *Ferroelectrics* (to be published).
- ³⁴Yu. M. Poplavko, *Fizika Dielektrikov* (Izd. Wysha Shkola, Kiev, 1980), p. 291.
- ³⁵E. Hegenbarth, *Phys. Status Solidi* **6**, 333 (1964).
- ³⁶B. Westwanski, A. Ogaza, and B. Fugiel, *Phys. Rev. B* **45**, 2699 (1992); **45**, 2704 (1992).